Green Chemical Technology

SCIEPublish

Article

Eco-Friendly Synthesis of Spherical Lanthanum-Doped Hydroxyapatite from Phosphogypsum Waste: A High-Efficiency Strategy for Fluoride Removal in Aqueous Solutions

Shanzhu Jiang [1,2,†], Zhaobo Wang [2,*,†], Yangjie Qin [2], Bensanglang Cao [2] and Ruan Chi [1,2]

[1] Key Laboratory for Green Chemical Process of Ministry of Education, Wuhan Institute of Technology, Wuhan 430000, China; jiangshanzhu@hbsxsys.com (S.J.); rac@wit.edu.cn (R.C.)

[2] Phosphogypsum Utilization R&D Center, Hubei Three Gorges Laboratory, Yichang 443007, China; tanyangjie@hbsxsys.com (Y.Q.); caobensanglang@hbsxsys.com (B.C.)

* Corresponding author. E-mail: wangzhaobo@hbsxsys.com (Z.W.)

† These authors contributed equally to this work.

Received: 12 January 2026; Revised: 27 January 2026; Accepted: 23 March 2026; Available online: 3 April 2026

ABSTRACT: To address the environmental challenges posed by massive phosphogypsum (PG) stockpiles and groundwater fluoride contamination, this study developed an eco-friendly strategy for synthesizing lanthanum-doped hydroxyapatite (La-PGHAP) from PG waste via an acid precipitation-hydrothermal method. The synthesized La-PGHAP exhibited a spherical morphology, high crystallinity, and a significantly enhanced specific surface area of 53.11 m^2/g. Batch adsorption experiments revealed that pH critically influenced fluoride (F^-) removal, with maximum adsorption capacities of 8.20 mg/g (PGHAP) and 31.98 mg/g (La-PGHAP) at pH 4. The adsorption process followed pseudo-second-order kinetics and the Langmuir isotherm model, indicating chemisorption-dominated monolayer adsorption. La doping introduced Lewis acid-base interactions through La^{3+}–F^- coordination, improving both adsorption capacity and stability across a wide pH range (2–10). Reusability tests demonstrated that La-PGHAP retained 85.4% of its initial capacity after 4 cycles. This "waste-to-waste" approach not only repurposes PG into a high-efficiency adsorbent but also provides a sustainable solution for mitigating fluoride pollution, showcasing significant potential for industrial-scale water treatment applications.

Keywords: Phosphogypsum; Hydroxyapatite; Lanthanum-doped; Fluorine ion; Adsorption

1. Introduction

Phosphogypsum (PG), a byproduct of phosphoric acid production via the wet process, contains calcium sulfate dihydrate ($CaSO_4 \cdot 2H_2O$) along with impurities such as residual phosphate rock (3–8% P_2O_5), fluoride (1.2–4.5%), heavy metals (e.g., Cd, As), and trace radionuclides [1]. China, the world's largest PG

producer, generates over 80 million tons annually, with cumulative stockpiles exceeding 800 million tons as of 2022. As China's leading phosphate chemical hub, Hubei holds the nation's largest phosphate rock reserves and fertilizer output. It generates nearly 30 million tons of phosphogypsum each year, making it the country's leading source of accumulated waste. The primary factors restricting the comprehensive utilization of phosphogypsum are its high impurity content and the low economic competitiveness of its related products. Only 50% of the PG is currently utilized, primarily in low-value applications like cement retardants (33%) and soil amendments (2%), while the rest is landfilled, posing severe ecological risks through acidic leachate (pH 1.5–4.5) and fluoride migration into groundwater [2,3]. Fluoride contamination from PG stockpiles and natural sources affects 37 million people in China, particularly in Shaanxi and Xinjiang, where groundwater F^- concentrations reach 6–30 mg/L [4]. Chronic exposure to 3–6 mg/L F^- causes dental fluorosis (mottled enamel) and skeletal fluorosis (bone deformation), as confirmed by epidemiological studies showing 42% prevalence in endemic areas [5].

Conventional PG recycling faces three key bottlenecks: (1) The application of building materials (such as gypsum board) is facing market resistance due to user acceptance issues, approximately 3000 tons of phosphogypsum are consumed annually through this pathway [6,7]; (2) Soil amendment requires costly transportation and shows inconsistent crop yield improvement (*vs*. commercial fertilizers), around 600 tons of phosphogypsum are consumed annually through this pathway [8,9]; (3) Chemical conversion to high-value products (e.g., $(NH_4)_2SO_4$) demands energy-intensive fluoride removal (>90% purity required), approximately 400 tons of phosphogypsum are consumed annually through this pathway [10]. Despite the above approaches, the full utilization of phosphogypsum remains challenging given its annual production volume. In order to achieve "waste for waste" comprehensive treatment model, HAP synthesized by chemical conversion of PG (PGHAP) to adsorb and remove F^- in water is a novel resourceful utilization. HAP is a calcium phosphate biomaterial with the chemical formula $Ca_{10}(PO_4)_6(OH)_2$. There are two different binding sites C and P on the surface, the C site composed of Ca^{2+} is positively charged, and the P site composed of PO_4^{3-} group is negatively charged [11]. The adsorption of F^- by HAP is mainly based on its unique physicochemical properties and structural characteristics, and it has become a research hotspot in recent years as a new type of environmentally functional material. Specifically, it can be summarized as Ca^{2+} in HAP reacting with F^- in solution to produce CaF_2 precipitation, or F^- replacing some of the hydroxyl group (-OH) in HAP to form fluorapatite ($Ca_5(PO_4)_3F$), or F^- adsorbing on the surface of HAP by electrostatic and van der Waals forces. However, pure HAP exhibits limited adsorption capacity and selectivity for fluoride under complex aqueous conditions, necessitating structural modifications to enhance its performance. Experimental studies reveal that unmodified HAP achieves an adsorption capacity of only 6.88–10.9 mg/g [12,13]. This constraint arises from the inherent structural limitations of pure HAP, including its low specific surface area, limited active sites for F^- binding, and susceptibility to surface charge reversal in acidic or alkaline media [14].

To address these challenges, structural modifications of HAP have emerged as a critical strategy to enhance both adsorption capacity and selectivity. Spherical HAP achieved a synergistic improvement in specific surface area, diffusion kinetics, and active site density through geometric morphology optimization, and its adsorption capacity and rate were significantly better than non spherical structures [15]. In addition, doping with multivalent cations (e.g., La^{3+}, Zn^{2+}, Mg^{2+}) has been shown to optimize the crystallinity and surface chemistry of HAP. For example, La^{3+}-doped HAP introduces strong Lewis acid-base interactions between La^{3+} and F^-, increasing adsorption capacity while maintaining stability across a pH range of 4–10 [16]. Based on this, this work pioneers the integration of industrial solid waste recycling with advanced adsorbent design, offering a dual solution to fluoride pollution and phosphogypsum accumulation. Advanced characterization techniques (XRD, XPS, and BET) are employed to elucidate the structural evolution and fluoride binding mechanisms. The La-PGHAP composite material is expected to exhibit excellent adsorption capacity compared to conventional HAP, while maintaining stability across a wide pH

range. The findings are expected to advance the development of eco-friendly water treatment materials and provide actionable insights for scaling up PG-based adsorbents in industrial applications.

2. Materials and Methods

2.1. Materials and Reagents

A chemical enterprise in Hubei Province, China supplied PG. Potassium phosphate monobasic, hydrochloric acid, sodium hydroxide, and sodium fluoride were purchased from China National Medicines Group Chemical Reagents Co., Ltd. (Beijing, China).

2.2. Synthesis Process of Adsorbent Materials

Raw phosphogypsum (50 g) was subjected to acid leaching by stirring with 250 mL of 2 mol/L hydrochloric acid at 80 °C for 2 h, followed by vacuum filtration through a 0.45 μm polyethersulfone membrane to remove insoluble impurities (e.g., silica and residual phosphate rock). The filtrate was rapidly cooled to 25 °C in an ice-water bath to precipitate calcium-rich solids, which were collected via centrifugation (6000 rpm, 10 min) and redispersed in deionized water to form a homogeneous Ca^{2+} suspension. This calcium source was combined with a 0.5 mol/L potassium dihydrogen phosphate (KH_2PO_4) solution at a stoichiometric Ca:P molar ratio of 1.67, followed by sequential addition of urea (urea:Ca = 10:1 mol/mol) and EDTA (0.03 mol/L final concentration) to regulate crystal growth kinetics. The mixture pH was adjusted to 3.0 ± 0.1 using diluted HNO_3 to prevent premature hydroxyapatite nucleation [17]. For La-doped samples, predetermined quantities of La_2O_3 (corresponding to La:Ca molar ratios of 1%, 3%, and 5%) were dissolved in 5 mL concentrated HNO_3 before incorporation into the reaction system. The precursor solution was transferred into a 100 mL Teflon-lined stainless steel autoclave and hydrothermally treated at 150 °C for 8 h under autogenous pressure (0.85 bar), during which urea decomposition ($NH_2CONH_2 \rightarrow 2NH_3 + CO_2$) gradually elevated the pH to ~9.5, enabling controlled crystallization. Post-synthesis, the products were vacuum-filtered, washed alternately with deionized water and ethanol to eliminate ionic residues and organic byproducts, and dried overnight at 60 °C in a vacuum oven to obtain PGHAP and La-PGHAP powders (see Figure 1).

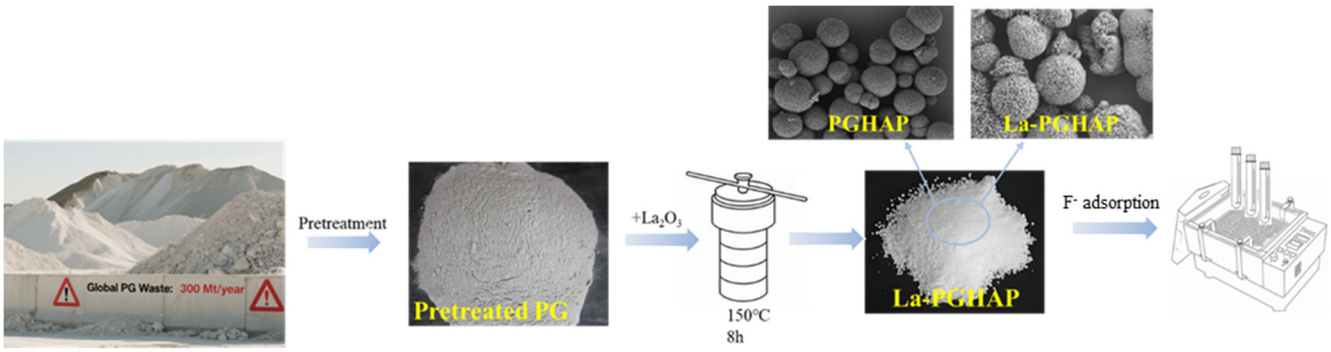

Figure 1. Synthesis process of adsorbent material.

2.3. Static Batch Adsorption Test

In the static batch adsorption test, the control variable method was used to control only variables, including adsorption time, F^- initial concentration, temperature, pH, and adsorbent dosing. Specifically, a certain mass of adsorbent (10–50 mg) was added to a 50 mL conical flask, and then 20 mL of F^- solutions (10, 20, 30, 40, and 50 mg/L) with different concentrations having different pH (2, 4, 6, 8, and 10) were added. The static adsorption test was carried out in a thermostatic water bath shaker set at 200 rpm, and the thermostatic oscillator was set at different temperatures (25, 30, 35, 40, and 45 °C), and the concentration

of F^- in the supernatant was determined by ion chromatography. The above experiments were repeated three times to take the average value.

2.4. Calculation and Analytical Methods

The amount of F^- adsorbed by the adsorbent at time t (q_t, mg/g) and the amount adsorbed at the equilibrium moment (q_e, mg/g) were calculated by Equation (1) and Equation (2), respectively.

$$q_t = \frac{(c_0 - c_t)V}{M} \tag{1}$$

$$q_e = \frac{(c_0 - c_e)V}{M} \tag{2}$$

where c_0 is the initial F^- concentration, mg/L; c_t is the concentration of F at time t, mg/L; c_e is the F^- concentration at the equilibrium moment, mg/L; M is the adsorbent dosage, g; V is the volume of F-solution, L.

The dynamic curves were fitted by pseudo-first-order and pseudo-second-order kinetic models, and the kinetic parameters, such as pseudo-first-order rate constant (k_1, h^{-1}), pseudo-second-order rate constant (g/mg·h), the theoretical adsorption capacity (q_{e0}, mg/g), and the number of data points (n) were calculated. The isotherm curves were fitted by the Freundlich and Langmuir model, and the thermodynamic parameters, such as Gibbs energy (ΔG, $kJ \cdot mol^{-1}$), enthalpy (ΔH, $kJ \cdot mol^{-1}$) and entropy [ΔS, $J \cdot (mol \cdot K)^{-1}$] were calculated according to Equations (3)–(5). R is the ideal-gas constant, 8.314 $J \cdot (mol \cdot K)^{-1}$.

$$\Delta G^0 = -RT\ln K_0 \tag{3}$$

$$\ln K_0 = \frac{\Delta S^0}{R} - \frac{\Delta H^0}{RT} \tag{4}$$

$$\Delta S = \frac{\Delta H - \Delta G}{T} \tag{5}$$

3. Results and Discussion

3.1. Morphological and Compositional Analysis of La-PGHAP

The SEM images in Figure 2 vividly illustrate the series of dynamic morphological changes induced by the gradual increase of La doping concentration. The undoped PGHAP (Figure 2a) serves as a reference, exhibiting well-defined, smooth spherical particles approximately 2–3 μm in diameter. Upon introducing a low La doping level (1%, Figure 2b), the first significant morphological transition occurs. The originally smooth surfaces of the microspheres are uniformly decorated with sub-100 nm protrusions. This phenomenon is attributed to La^{3+}-mediated heterogeneous nucleation, marking the initial stage where La incorporation begins to alter the crystal growth habit. As the doping concentration is raised to 3% (Figure 2c), a more profound transformation takes place. The primary particles lose their individual spherical identity and aggregate into larger clusters ranging from 5 to 7 μm. This aggregation is primarily driven by the charge imbalance created by the substitution of Ca^{2+} with La^{3+} (as evidenced by the decrease in Ca content from 11.61 at.% to 8.09 at.% in Table 1), which is consistent with the charge compensation mechanism ($3Ca^{2+} \rightarrow 2La^{3+}$ + vacancy). Notably, at the highest doping level of 5% (Figure 2d), the morphology undergoes a final, distinct evolution. The structure develops pronounced porosity with pore sizes around 200 nm, and the overall particle size is reduced to 1–5 μm. This unique architecture is likely the result of synergistic effects involving surface precipitation of $La(OH)_3$ and significant lattice strain due to the ionic radius mismatch between Ca^{2+} and La^{3+}. Importantly, the highly porous and rugged morphology observed at 3% and 5% La doping is anticipated to provide a larger specific surface area and more active

sites, which is highly favorable for the subsequent fluoride adsorption process discussed in the following sections [17,18].

EDS data (Table 1) quantify doping inefficiency: La atomic percentages (0.16–0.24 at.%) remain far below theoretical values (1–5%), indicating limited lattice incorporation (<25% doping efficiency) and preferential La^{3+} surface enrichment. Concurrently, phosphorus depletion at 5% La (2.97 at.% *vs*. 6.70 at.% in 1% La-PGHAP) suggests $LaPO_4$ phase formation, while oxygen content stability (26.01–26.98 at.%) confirms maintained apatitic structure. Carbon contamination (47.81–65.06 at.%) likely originates from urea decomposition residues. These findings collectively demonstrate that La doping modifies both surface chemistry (La–O–F coordination sites) and textural properties (mesoporosity), synergistically enhancing fluoride adsorption potential despite suboptimal dopant integration [19,20].

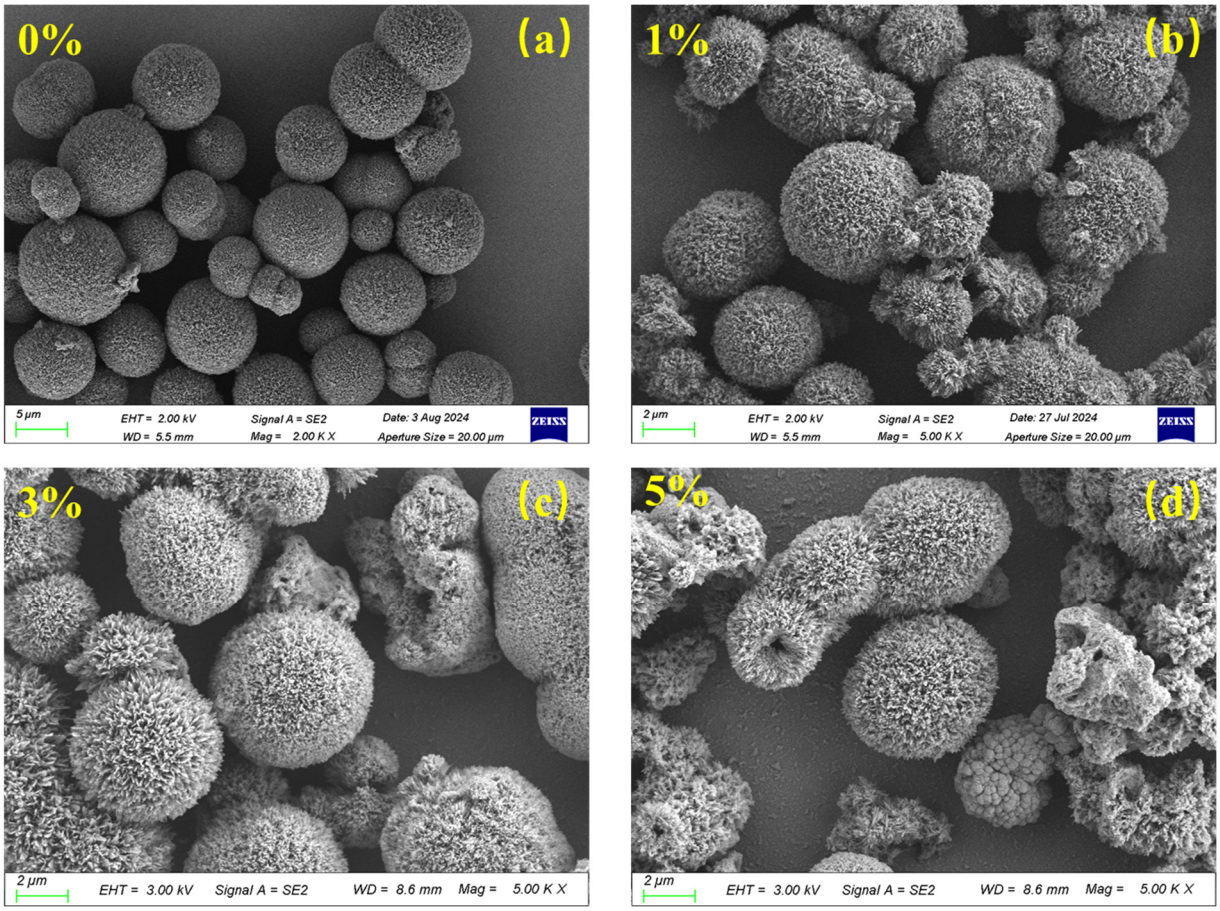

Figure 2. SEM images of PGHAP and La-PGHAP with different La contents: (**a**) 0%; (**b**) 1%; (**c**) 3%; (**d**) 5%.

Table 1. Average atom percentage of cations of samples by EDS.

	Element Content (at.%)				
Doping Amount	**C**	**O**	**P**	**Ca**	**La**
PGHAP	60.25	21.28	7.05	11.42	0
1% La-PGHAP	55.61	26.01	6.70	11.61	0.16
3% La-PGHAP	47.81	38.67	5.20	8.09	0.23
5% La-PGHAP	65.06	26.98	2.97	4.75	0.24

3.2. Structural and Textural Characterization of PGHAP and La-PGHAP

XRD analysis (Figure 3a) confirms the dual-phase composition of pristine PGHAP, exhibiting characteristic diffraction peaks of both $CaSO_4 \cdot 2H_2O$ (2θ = 11.6°, 20.7°, 23.4°) and hydroxyapatite (HAP,

JCPDS 09-0432, 2θ = 25.9°, 31.8°, 49.5°), demonstrating incomplete conversion of phosphogypsum during synthesis. The coexistence of these phases suggests residual sulfate groups from the PG precursor, consistent with its industrial origin. Upon La doping (Figure 3b), the HAP phase remains dominant across all La-PGHAP samples (1–5% La), indicating successful La^{3+} incorporation into the HAP lattice. Notably, the (002) peak at 25.9° progressively broadens (FWHM increases from 0.38° to 0.61°) and shifts to lower angles (25.9° → 25.6°) with higher La loading, confirming La^{3+} substitution at Ca^{2+} sites (ionic radius mismatch) and resultant lattice expansion along the *c*-axis.

N_2 adsorption-desorption isotherms (Figure 3c) reveal a systematic enhancement in textural properties with La doping. All samples display Type IV isotherms with H3 hysteresis loops (P/P_0 = 0.45–0.95), indicative of mesoporous structures formed by nanoparticle aggregation. The BET surface area (Table 2) increases dramatically from 24.55 m^2/g (PGHAP) to 53.11 m^2/g (5% La-PGHAP), while total pore volume rises from 0.1412 cm^3/g to 0.2491 cm^3/g, attributable to La^{3+}-induced inhibition of HAP crystallite growth and formation of interparticle voids. Corresponding pore size distributions (Figure 3d) demonstrate a progressive shift from broad macroporous dominance (PGHAP: the average pore size of the mesopores is 36.59 nm) to narrower mesoporous regimes (5% La-PGHAP: the average pore size of the mesopores is 18.97 nm), corroborated by decreasing average mesopore size (22.99 → 18.76 nm) and micropore volume reduction (0.00562 → 0.00197 cm^3/g). This textural evolution (enhanced mesoporosity coupled with reduced microporosity) optimizes mass transfer kinetics for adsorbate diffusion while maximizing accessible active sites.

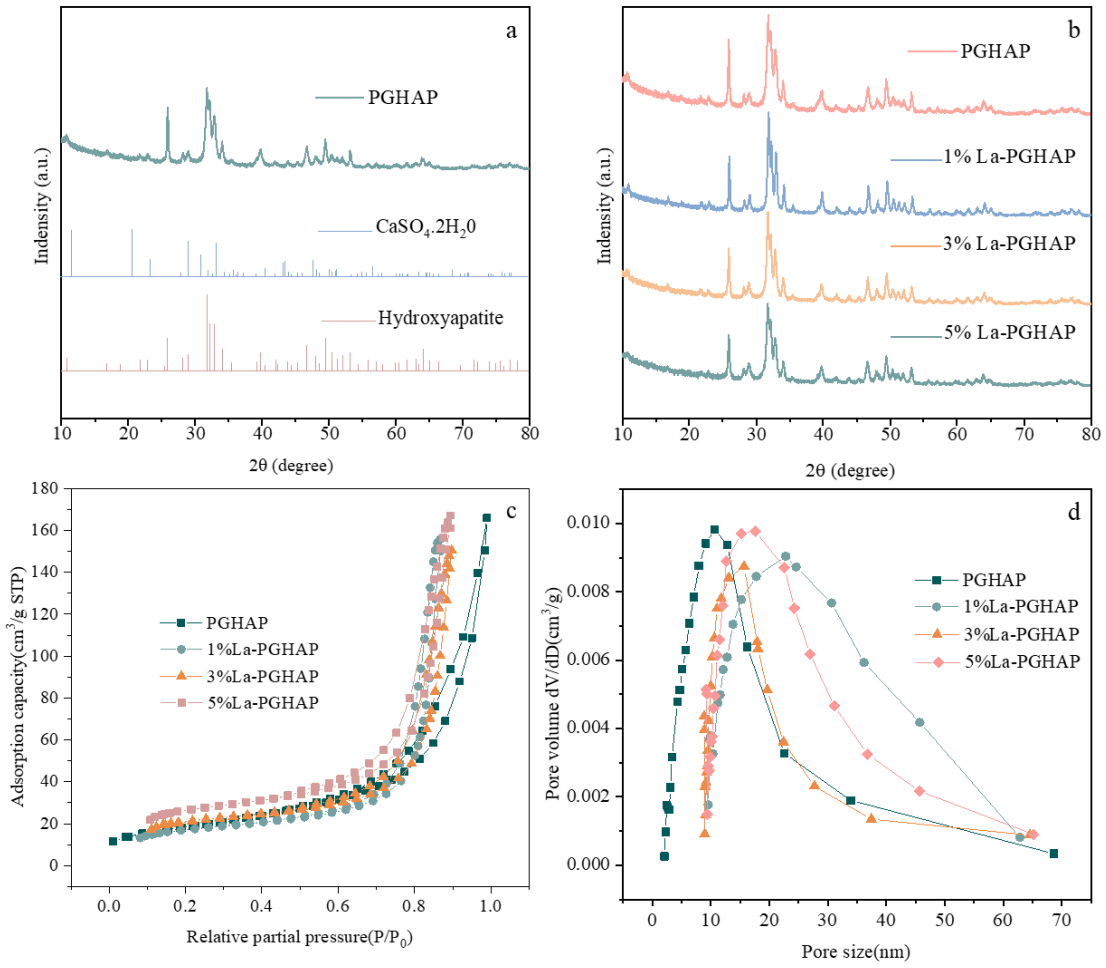

Figure 3. (**a**) XRD characterization of PGHAP, $CaSO_4 \cdot 2H_2O$, hydroxyapatite; (**b**) XRD characterization of PGHAP and 1–5% La-PGHAP; (**c**) N_2 adsorption-desorption diagram of PGHAP and 1–5% La-PGHAP; (**d**) pore size distribution of PGHAP and 1–5% La-PGHAP.

Table 2. The specific surface area and pore structure table before and after material synthesis.

Samples	BET Specific Surface Area	Specific Surface Area in Micropores	Extraporeal Specific Surface Area	Total Pore Volume	Micropore Volume	Average Pore Size	Average Pore Size of Mesopores
	m^2/g	m^2/g	m^2/g	cm^3/g	cm^3/g	nm	nm
PGHAP	24.5501	13.4632	11.0869	0.1412	0.00562	22.9979	36.5950
1% La-PGHAP	38.6148	3.8452	34.7696	0.2412	0.00115	24.9903	26.4742
3% La-PGHAP	46.8563	4.9055	41.9507	0.2549	0.00140	21.7560	23.4647
5% La-PGHAP	53.1108	5.9231	47.1877	0.2491	0.00197	18.7590	18.9746

3.3. Multivariate Adsorption Performance of PGHAP and La-PGHAP

As evidenced by the adsorption results (Figure 4), La doping significantly enhances the fluoride (F^-) uptake capacity of phosphogypsum-derived hydroxyapatite (PGHAP) in a dose-dependent but non-linear manner. At 0% La doping (pristine PGHAP), the adsorption capacity reaches 2.10 mg/g (under non optimal adsorption conditions), attributed to conventional mechanisms including ion exchange ($OH^- \rightarrow F^-$) and electrostatic attraction at Ca^{2+} sites. Upon introducing 1% La, the capacity surges to 2.55 mg/g (under the same adsorption conditions), demonstrating that La^{3+} doping creates additional Lewis acid-base interaction sites—La^{3+} coordinates strongly with F^- through inner-sphere complexation. This aligns with studies showing La–O–F bond formation enhances chemisorption efficiency. The incremental gain diminishes at 3% La doping (3.1 mg/g, +23.5% *vs*. 1% La-PGHAP), and the adsorption capacity for fluoride ions reaches its maximum. Notably, the plateau at 5% La (2.9 mg/g) indicates two competing effects: (1) Excessive La loading (>3%) may induce particle agglomeration, reducing effective surface area; (2) Formation of $La(OH)_3$ surface precipitates at high doping levels could block mesopores, as evidenced by the unchanged capacity despite increased La content. The observed performance hierarchy (5% ≈ 3% > 1% > 0% La) under fixed experimental conditions (10 mg/L F^-, 25 °C, 50 mg adsorbent) highlights optimal doping at 3% La. This balance maximizes La^{3+} active site density while maintaining structural integrity. The pH-dependent zeta potential would strengthen electrostatic F^- attraction, though competitive anion effects (e.g., Cl^-) warrant further investigation. Therefore, 3% lanthanum doping was set as the optimum condition (all subsequent references to La-PGHAP are considered to be 3% lanthanum doping).

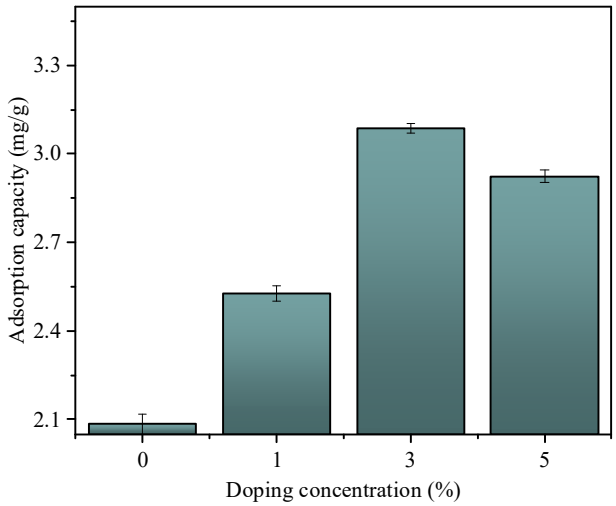

Figure 4. Adsorption capacity of adsorbent materials with different La doping levels for fluoride ions under the same conditions (pH 7.0, 50 mL F^- solution at 10 mg/L, 50 mg adsorbent, 25 °C).

In order to investigate the influence of different factors on adsorption properties, the multivariate adsorption behavior of PGHAP and La-PGHAP toward fluoride ions (F^-) was systematically investigated under six operational parameters (Figure 5), revealing fundamental divergences in adsorption mechanisms

mediated by La^{3+} doping. La-PGHAP exhibits significantly enhanced fluoride adsorption performance compared to pristine PGHAP across all tested conditions, with mechanistic divergences rooted in La^{3+} doping effects. Adsorption kinetics (Figure 5a) show that both materials exhibit rapid initial adsorption (0–50 min), La-PGHAP achieves a higher saturation capacity, attributed to La^{3+}-mediated chemisorption, reflecting optimized pore accessibility in La-doped mesostructures [21]. Adsorption capacity inversely correlates with dosage due to particle aggregation effects. Dosage dependence (Figure 5b) demonstrates La-PGHAP's superior site accessibility, La-PGHAP achieves 8.10 mg/g, 3.3× higher than PGHAP's 2.44 mg/g, demonstrating superior site availability, while its mesoporous structure mitigates aggregation-induced capacity loss slope.

pH sensitivity (Figure 5c) was studied in the range of 2–10, the adsorption of F^- by PGHAP and La-PGHAP (collectively referred to here as HAP) reached a maximum value at pH 4. Thereafter, the adsorption of F^- by HAP decreased as the pH continued to increase, which may be attributed to the fact that the hydroxyl groups on the HAP surface can release hydroxide ions in acidic solution, thereby making the surface positively charged. At this time, HAP and negatively charged F^- ions were attracted to each other by electrostatic attraction, leading to an increase in adsorption in the solution. However, in neutral or alkaline environments, the charge on the surface of HAP may gradually become neutral or negative, thus reducing the adsorption of F^- due to the presence of electrostatic repulsion. Meanwhile, at low pH, F^- in solution existed mainly as free ions, which was due to the high concentration of H^+ produced by the ionization of water under acidic conditions, making F^- less likely to form complexes with other ions. At high pH, F^- may form HF_2^- with OH^- in the water, this may also contribute to the decrease in adsorption [22,23].

F^- concentration response (Figure 5d) shows La-PGHAP's linear capacity scaling to its maximum at 30 mg/L, outperforming PGHAP's plateau at this point due to La^{3+}'s multidentate binding capability [24]. Temperature activation (Figure 5e) confirms the endothermic nature of both materials. Adsorption increases endothermically for both materials. At 40 °C, La-PGHAP achieves 29.35 mg/g (3.7× PGHAP's 7.90 mg/g), as thermal energy facilitates La–F inner-sphere complexation and pore expansion [25]. Ionic strength effects (Figure 5f) reveal La-PGHAP's exceptional NaCl tolerance, leveraging charge screening and high-selectivity ligand exchange, whereas PGHAP plateaus at 0.15 mg/L NaCl [26]. These results collectively demonstrate that the optimum adsorption conditions of F^- on La-PGHAP were 30 mg/L F^-, 0.2 g/L HAP dosage, 0.2 mg/L NaCl, pH 4, 40 °C, 150 min, and the maximum adsorption capacity could reach up to 31.98 mg/g, which was better than the results in other reports [23,27]. La doping transforms PGHAP from a diffusion-limited, pH-sensitive adsorbent into a robust multifunctional material with rapid kinetics, high capacity, and exceptional environmental resilience, positioning it as a next-generation solution for industrial fluoride remediation.

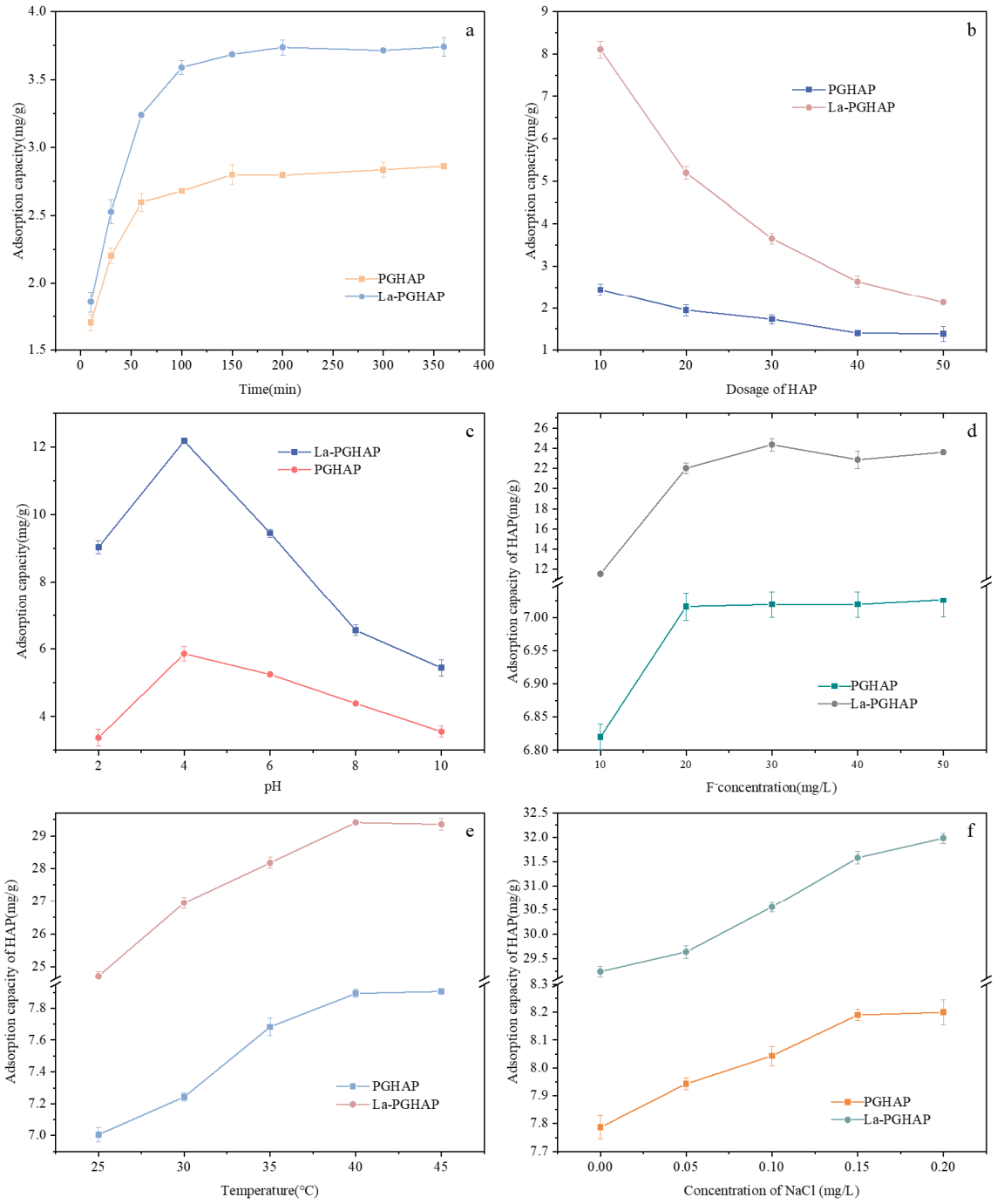

Figure 5. Effects of different factors on the F^- adsorption: (**a**) adsorption time; (**b**) dosage of adsorbent; (**c**) pH; (**d**) concentration of F^-; (**e**) temperature; (**f**) concentration of NaCl.

3.4. Adsorption Kinetics Analysis of PGHAP and La-PGHAP

In order to explore the adsorption mechanism of F^- on PGHAP and La-PGHAP, the adsorption kinetics of PGHAP and La-doped PGHAP were systematically investigated using pseudo-first-order (PFO) and pseudo-second-order (PSO) models (non-optimal conditions), as demonstrated in Figure 6 and Table 3. For pristine PGHAP, the experimental equilibrium adsorption capacity ($q_{e,exp}$) reached 2.86 mg/g, while La-PGHAP exhibited significantly enhanced performance ($q_{e,exp}$ = 3.71 mg/g), confirming the critical role of La^{3+} doping in optimizing active sites for fluoride capture [23,28].

The PSO model demonstrated superior fitting for both adsorbents, as evidenced by higher determination coefficients (PGHAP: R^2 = 0.9923 for PSO *vs*. R^2 = 0.8445 for PFO; La-HAP: R^2 = 0.9731

for PSO *vs*. R^2 = 0.8963 for PFO). This dominance of PSO kinetics implies chemisorption-driven mechanisms, likely involving strong La^{3+}-F^- coordination bonds and ion exchange at Ca^{2+} vacancies generated during La^{3+} substitution. The PSO rate constant (K_2) decreased from 0.04498 g/(mg·min) for PGHAP to 0.02123 g/(mg·min) for La-PGHAP, suggesting La doping slightly slowed the initial adsorption rate due to increased surface complexity and potential pore-blocking effects. However, the 30% enhancement in q_e for La-PGHAP compensates for this kinetic trade-off, aligning with its higher density of high-affinity La–O–F binding sites [23,28,29].

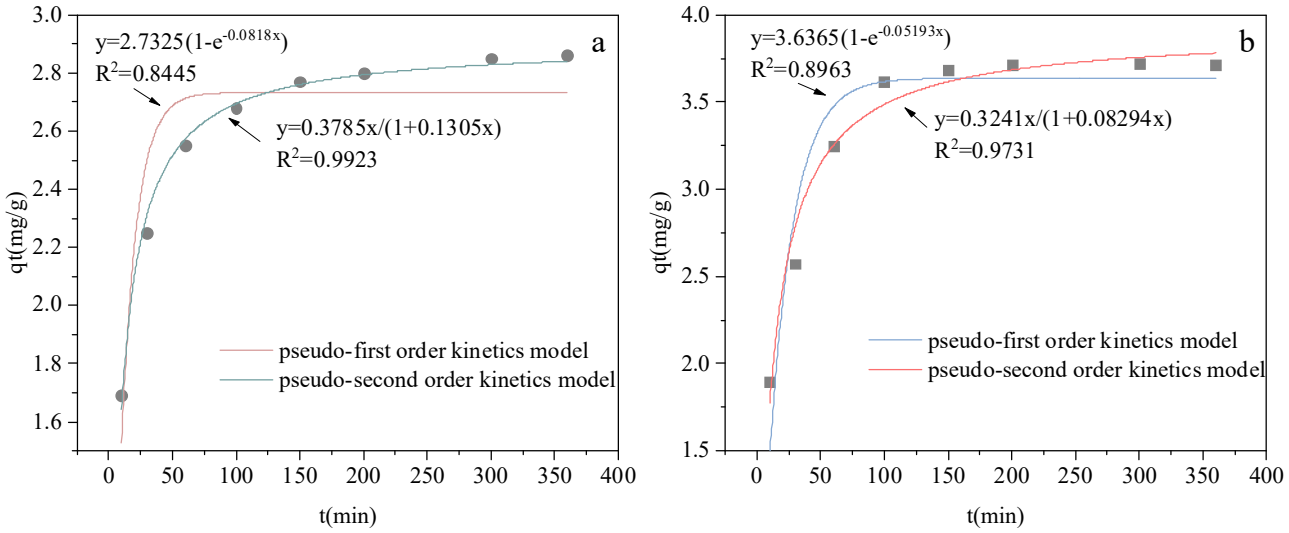

Figure 6. The fitting curve of adsorption kinetics of (**a**) PGHAP; (**b**) La-PGHAP.

Table 3. Adsorption kinetic parameters of PGHAP and La-PGHAP.

Model	Actual Adsorption Capacity	Pseudo-First-Order Kinetic		Pseudo-Second Order Kinetic			
Samples	**q_e (mg/g)**	**K_1**	**R^2**	**S**	**K_2**	**R^2**	**S**
PGHAP	2.86	0.0819	0.8445	0.1491	0.04498	0.9923	0.5249
La-PGHAP	3.71	0.05193	0.8963	0.2001	0.02123	0.9731	0.5958

3.5. Adsorption Isotherm Analysis of PGHAP and La-PGHAP

The adsorption equilibrium behavior of PGHAP and La-PGHAP was rigorously evaluated using Langmuir and the Freundlich isotherm models, as depicted in Figure 7 and Table 4. The Langmuir model exhibited exceptional fitting accuracy for both adsorbents across all temperatures ($R^2 > 0.9995$), suggesting monolayer adsorption dominated by homogeneous binding sites. In contrast, the Freundlich model showed significantly lower correlation coefficients (R^2 = 0.28–0.33 for La-PGHAP; R^2 = 0.69–0.88 for PGHAP), indicating limited applicability for describing multilayer or heterogeneous adsorption processes. The F^- on La-PGHAP adsorption process was more consistent with the assumption of monolayer adsorption. The Langmuir model assumed that the adsorbent surface was homogeneous, and that only one adsorbent molecule can be adsorbed at each adsorption site, and that cascading adsorption does not occur after saturation. The high degree of fit suggested that the adsorption sites on the adsorbent surface were independent and unresponsive to each other.

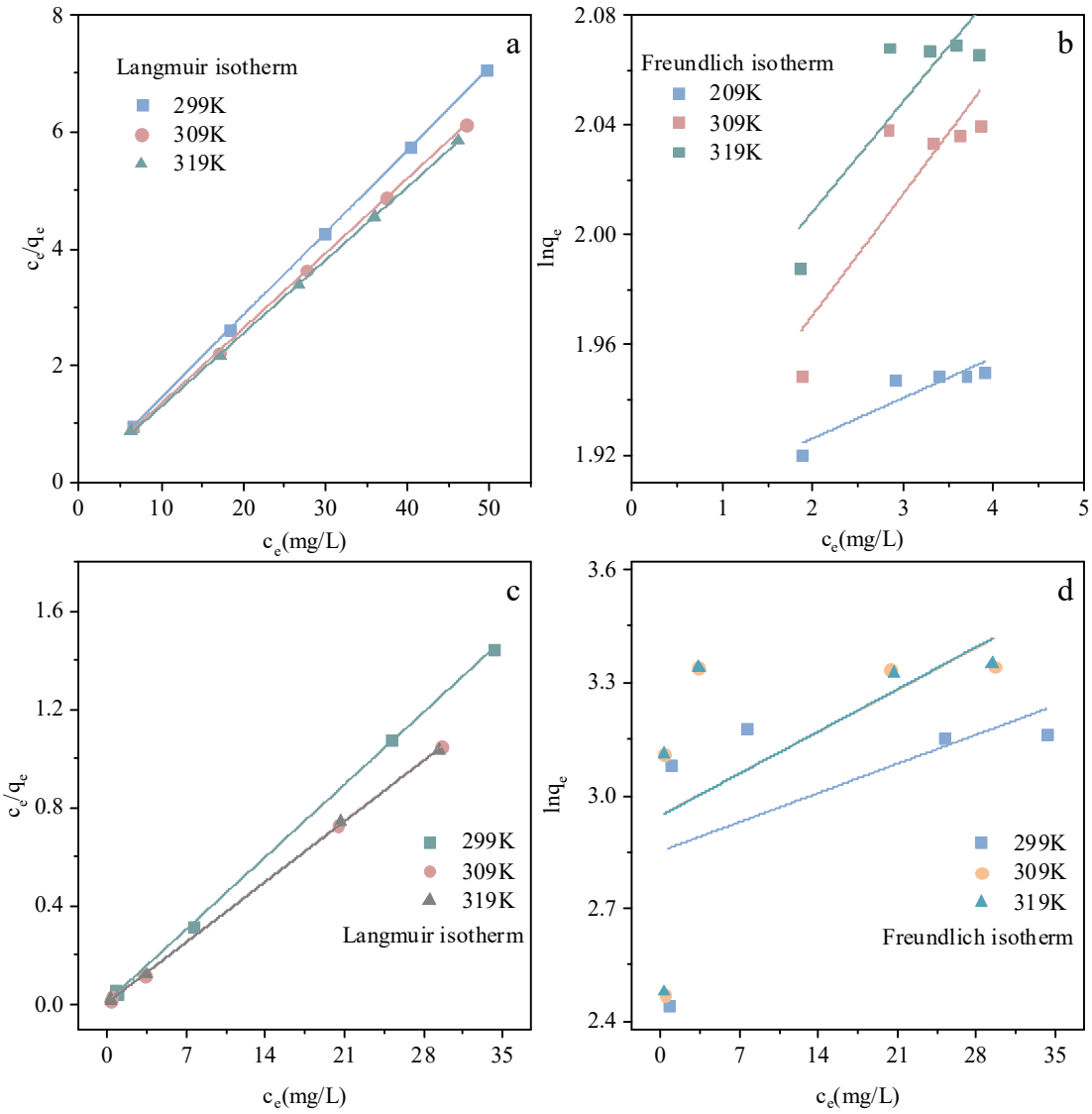

Figure 7. Fitting curves of F^- adsorption isotherm of (**a**,**b**) PGHAP; (**c**,**d**) La-PGHAP.

Remarkable q_{max} enhancement of La-PGHAP was observed (23.81–28.49 mg/g), with K_L increasing from 3.36 (298 K) to 4.62 (318 K). The positive temperature dependence of K_L aligns with chemisorption mechanisms, where La^{3+}–F^- coordination bonds strengthen through endothermic activation. In addition, it also implied that the adsorption energy was homogeneous rather than energetically diverse as described by the Freundlich model. This may be related to the crystal structure and surface properties of La-PGHAP, allowing F^- to form a uniform and energetically homogeneous monolayer adsorption on the surface [30–32].

Table 4. Adsorption isotherm model parameters of PGHAP and La-PGHAP.

Sample	Model	Langmuir Isotherm Model			Freundlich Isotherm Model		
	Temperature (K)	q_{max} (mg/g)	K_L (L/mg)	R^2	K_F (mg/g(L/mg)1/n)	n	R^2
PGHAP	298	19.22	5.56	0.9999	6.6619	67.80	0.8775
	308	15.55	1.99	0.9998	6.5693	22.65	0.7699
	318	21.53	2.69	0.9998	6.8806	25.04	0.6933
La-PGHAP	298	23.8095	3.36	0.9995	16.5196	8.3612	0.2822
	308	28.4900	4.2289	0.9997	19.7379	8.0386	0.3206
	318	28.4900	4.6184	0.9996	19.8518	7.9936	0.3308

3.6. Adsorption Thermodynamics Analysis of PGHAP and La-PGHAP

The thermodynamic parameters derived from Van't Hoff plots (Figure 8a,b) and Table 5 reveal distinct adsorption mechanisms for PGHAP and La-PGHAP. For pristine PGHAP, the positive enthalpy change (ΔH = +4.16 kJ/mol) and modest entropy gain (ΔS = +14.17 J/(mol·K)) indicate a weakly endothermic process dominated by physical interactions (e.g., electrostatic attraction or ion exchange), where the slight spontaneity (ΔG = −0.085 to −0.370 kJ/mol) and low equilibrium constants ($\ln K_L$ = 0.034–0.139) reflect limited F^- binding affinity. In stark contrast, La-PGHAP exhibits dramatically enhanced thermodynamic driving forces, with ΔH surging to +35.06 kJ/mol and ΔS escalating to +140.89 J/(mol·K), signifying a chemisorption-dominated mechanism involving high-energy La^{3+}–F^- coordination bonds. The strongly negative ΔG values (−6.96 to −9.76 kJ/mol) and the exponential $\ln K_L$ dependence on temperature (2.80–3.68) confirm that La doping transforms adsorption into a thermally activated process, in which elevated temperatures (299–319 K) facilitate La^{3+} site activation and F^- desolvation. The 8.4-fold ΔH amplification and 9.9-fold ΔS enhancement upon La incorporation quantitatively validate synergistic effects of chemical bond formation (La–F) and interfacial restructuring, establishing La-PGHAP as a temperature-responsive adsorbent optimized for high-temperature fluoride remediation [33–38].

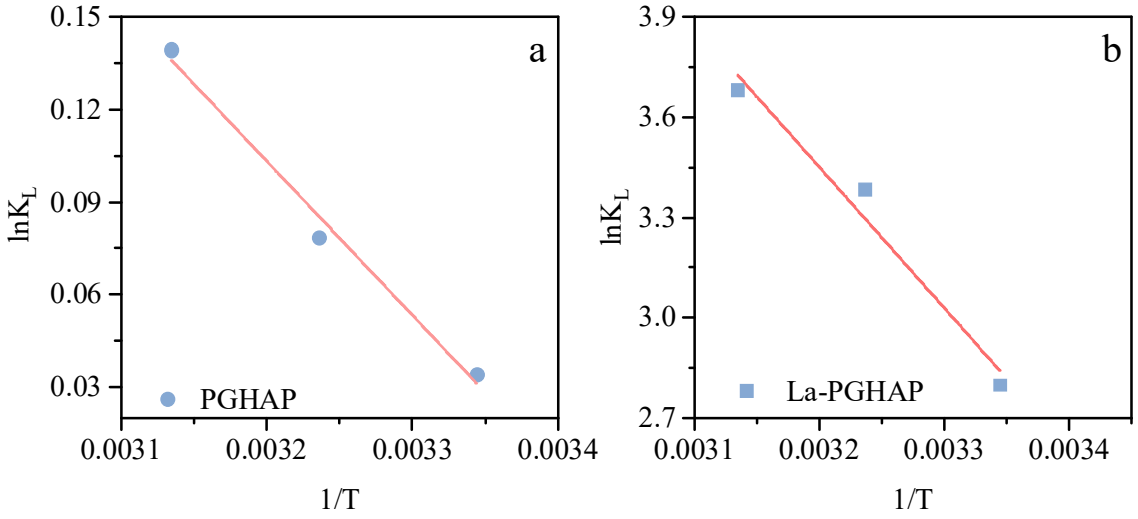

Figure 8. Linear regression of the thermodynamics of F^- adsorption of (**a**) PGHAP; (**b**) La-PGHAP.

Table 5. Thermodynamic parameters of adsorption onto PGHAP and La-PGHAP at different temperatures.

Sample	T/K	$\ln K_L$	R^2	ΔG/kJ·mol^{-1}	ΔS/J·(mol·K)$^{-1}$	ΔH/kJ·mol^{-1}
PGHAP	299	0.0343	0.9879	−0.0852	14.1687	4.1592
	309	0.0785		−0.2016		
	319	0.1394		−0.3697		
La-PGHAP	299	2.799891	0.9719	−6.9602	140.889	35.0610
	309	3.385237		−8.6967		
	319	3.681351		−9.7635		

3.7. Reusability Analysis of PGHAP and La-PGHAP

Reusability was an important performance parameter of adsorbents, and multiple reuse can reduce the cost of industrial applications [39]. The reusability evaluation over 10 adsorption-desorption cycles was shown in Figure 9. For pristine PGHAP, the adsorption capacity exhibited a continuous decline from 7.89 mg/g (Cycle 1) to 6.68 (Cycle 4) and 3.41 mg/g (Cycle 10), retaining 84.6% and 43.2% of its initial capacity. La-PGHAP demonstrated markedly enhanced cyclic stability, with capacity decreasing from 29.48 mg/g to 25.17 (Cycle 4) and 14.15 mg/g (Cycle 10), retaining 85.4% and 48.0% of its initial capacity, despite its

higher initial adsorption performance [40,41]. The divergence in decay patterns (PGHAP's rapid linear decline versus La-PGHAP's biphasic decay) reveals La^{3+}'s dual role in enhancing durability: (1) La–O bonds resist acid corrosion more effectively than Ca–O bonds, reducing active site loss; (2) La^{3+} doping introduces lattice distortions that inhibit hydroxyapatite recrystallization during regeneration, preserving mesoporous structures. While La-PGHAP's absolute capacity loss exceeds PGHAP's, its residual capacity remains higher than PGHAP's, demonstrating the critical trade-off between initial performance and long-term usability [42,43].

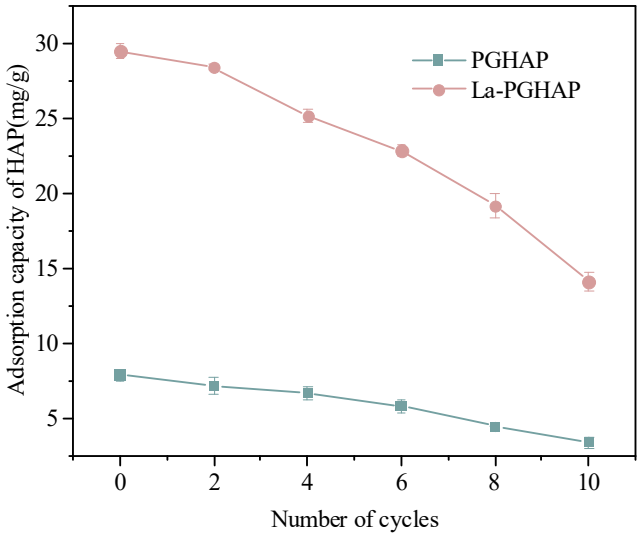

Figure 9. Reusability of PGHAP and La-PGHAP.

4. Conclusions

This study successfully synthesized lanthanum-doped hydroxyapatite (La-PGHAP) from phosphogypsum (PG) waste, demonstrating its efficacy as a high-performance adsorbent for fluoride removal. Key findings include the acid precipitation-hydrothermal method enabled the conversion of PG into La-PGHAP with a well-defined spherical structure, high crystallinity, and a mesoporous architecture. La^{3+} doping enhanced surface reactivity and introduced additional adsorption sites via strong La^{3+}–F^{-} interactions. Maximum F^{-} adsorption capacity reached 31.98 mg/g under optimal conditions (pH 4, 40 °C), outperforming conventional hydroxyapatite. Adsorption mechanisms were dominated by chemisorption, as evidenced by the fits to pseudo-second-order kinetics and the Langmuir isotherm model. In addition, La-PGHAP exhibited robust performance over a broad pH range (2–10) and maintained 85.4% of its adsorption capacity after 4 regeneration cycles, highlighting its stability and reusability. The "waste-to-waste" strategy not only addresses PG disposal challenges but also provides a cost-effective solution for remediation of fluoride-contaminated water. The integration of industrial waste recycling with advanced adsorbent design positions La-PGHAP as a promising candidate for large-scale environmental applications, aligning with the Sustainable Development Goals.

Statement of the Use of Generative AI and AI-Assisted Technologies in the Writing Process

During the preparation of this manuscript, the author(s) used Deepseek in order to optimize the logical flow of the manuscript structure, refine English expression accuracy, and check for grammatical and typographical errors. After using these tools, the author(s) thoroughly reviewed and edited the content, verified all scientific data, experimental details, and conclusion validity, and take(s) full responsibility for the content of the published article.

Acknowledgements

The authors gratefully acknowledge financial support from the Natural Science Foundation of Hubei Province (Grant No. 2025AFD245), and the Natural Science Foundation of Yichang Municipality (Grant No. A24-3-043). The authors extend their gratitude to Scientific Compass (www.shiyanjia.com, accessed on 8 July 2025) for providing invaluable assistance with characterization analysis.

Author Contributions

Conceptualization, Z.W.; Methodology, S.J.; Investigation, S.J. and Y.Q.; Resources, Z.W., B.C. and R.C.; Data Curation, S.J. and Y.Q.; Writing—Original Draft Preparation, S.J.; Writing—Review & Editing, Z.W.; Visualization, B.C.; Supervision, Z.W. and R.C.; Project Administration, Z.W.; Funding Acquisition, Z.W.

Ethics Statement

"Not applicable" for studies not involving humans or animals.

Informed Consent Statement

"Not applicable" for studies not involving humans.

Data Availability Statement

The data used in this study are not publicly accessible and cannot be made available due to internal research policies.

Funding

This research was funded by the Natural Science Foundation of Hubei Province grant number 2025AFD245 and the Natural Science Foundation of Yichang Municipality grant number A24-3-043.

Declaration of Competing Interest

The authors declare that they have no known competing financial interests or personal relationships that could have appeared to influence the work reported in this paper.

References

1. Akfas F, Elghali A, Aboulaich A, Munoz M, Benzaazoua M, Bodinier J-L. Exploring the potential reuse of phosphogypsum: A waste or a resource? *Sci. Total Environ.* **2024**, *908*, 168196. DOI:10.1016/j.scitotenv.2023.168196
2. Fang K, Xu L, Yang M, Chen Q. One-step wet-process phosphoric acid by-product $CaSO_4$ and its purification. *Sep. Purif. Technol.* **2023**, *309*, 123048. DOI:10.1016/j.seppur.2022.123048
3. Wang M, Guo Z, Du J, Lu H, Liu L, Wang T, et al. Assessing the hepatotoxicity of phosphogypsum leachate in zebrafish (*Danio rerio*). *Sci. Total Environ.* **2024**, *926*, 172018. DOI:10.1016/j.scitotenv.2024.172018
4. Li B, Zhang L, Cheng M, Chen L, Fang W, Liu S, et al. Evaluation of fluoride emissions and pollution from an electrolytic aluminum plant located in Yunnan province. *J. Hazard. Mater.* **2024**, *478*, 135500. DOI:10.1016/j.jhazmat.2024.135500
5. Johnston NR, Strobel SA. Principles of fluoride toxicity and the cellular response: A review. *Arch. Toxicol.* **2020**, *94*, 1051–1069. DOI:10.1007/s00204-020-02687-5
6. Zeng L, Bian X, Weng J, Zhang T. Wetting-drying effect on the strength and microstructure of cement-phosphogypsum stabilized soils. *J. Rock Mech. Geotech. Eng.* **2024**, *16*, 1049–1058. DOI:10.1016/j.jrmge.2023.06.022
7. Ou L, Li R, Zhu H, Zhao H, Chen R. Upcycling waste phosphogypsum as an alternative filler for asphalt pavement. *J. Clean. Prod.* **2023**, *420*, 138332. DOI:10.1016/j.jclepro.2023.138332
8. Zhang J, Yu K, Yu M, Dong X, Tariq Sarwar M, Yang H. Facet-engineering strategy of phosphogypsum for production of mineral slow-release fertilizers with efficient nutrient fixation and delivery. *Waste Manag.* **2024**, *182*, 259–270. DOI:10.1016/j.wasman.2024.04.041

9. Liu X, Wu C, Lv W, Dong E, Fu S, Zhang L, et al. Regulating sulfur migration and transformation in low water-binder ratio cementitious system incorporating phosphogypsum aggregate: Environmentally friendly clean materials. *J. Build. Eng.* **2024**, *91*, 109586. DOI:10.1016/j.jobe.2024.109586
10. Sazali NN, Mohamed MA, Mohd Yusoff SF, Hasnan NSN, Nordin NA, Anuar NA, et al. Conversion of waste phosphogypsum into value-added 1D/2D homojunction hydroxyapatite with enhanced structural, morphology, and photoelectrochemical performance. *J. Environ. Chem. Eng.* **2024**, *12*, 112784. DOI:10.1016/j.jece.2024.112784
11. Adhikara AG, Maharani AP, Puspitasari A, Nuswantoro NF, Juliadmi D, Maras MAJ, et al. Bovine hydroxyapatite for bone tissue engineering: Preparation, characterization, challenges, and future perspectives. *Eur. Polym. J.* **2024**, *214*, 113171. DOI:10.1016/j.eurpolymj.2024.113171
12. Balasooriya IL, Chen J, Korale Gedara SM, Han Y, Wickramaratne MN. Applications of Nano Hydroxyapatite as Adsorbents: A Review. *Nanomaterials* **2022**, *12*, 2324. DOI:10.3390/nano12142324
13. Rathnayake A, Hettithanthri O, Sandanayake S, Mahatantila K, Rajapaksha AU, Vithanage M. Essence of hydroxyapatite in defluoridation of drinking water: A review. *Environ. Pollut.* **2022**, *311*, 119882. DOI:10.1016/j.envpol.2022.119882
14. Russo V, D'Angelo A, Salvi C, Paparo R, Fortunato ME, Cepollaro EM, et al. Fluoride adsorption on hydroxyapatite: From batch to continuous operation. *J. Environ. Chem. Eng.* **2024**, *12*, 111973. DOI:10.1016/j.jece.2024.111973
15. Qin Y, Wang Z, Jiang S, Chi R, Huang S, Ma H, et al. Synthesis of solid micro-spherical hydroxyapatite by hard-template method: Optimization and characterization. *J. Porous Mater.* **2025**, *32*, 741–751. DOI:10.1007/s10934-024-01731-4
16. Wimalasiri AKDVK, Fernando MS, Dziemidowicz K, Williams GR, Koswattage KR, Dissanayake DP, et al. Structure–Activity Relationship of Lanthanide-Incorporated Nano-Hydroxyapatite for the Adsorption of Fluoride and Lead. *ACS Omega* **2021**, *6*, 13527–13543. DOI:10.1021/acsomega.0c05935
17. Jiang S, Wang Z, Qin Y, Chi R, Huang S, Ma H, et al. Acid precipitation-hydrothermal synthesis of needle-like hydroxyapatite for protein adsorption from waste phosphogypsum. *Environ. Technol.* **2025**, *46*, 1718–1729. DOI:10.1080/09593330.2024.2402099
18. Wang C, Yuan X, Kang H, Yin R, Cai A, Yue Z, et al. Structural characterization, photothermal effect and biological properties of La/Ga ion co-doped hydroxyapatite coated with polydopamine. *J. Ind. Eng. Chem.* **2024**, *139*, 573–586. DOI:10.1016/j.jiec.2024.05.033
19. Gao L, Li Y, Li G, Huo J, Jia L. Interface charge induced self-assembled $(Co(OH)_2)4$@$La(OH)_3$ heterojunction derived from Co4-MOF@$La(HCO_2)_3$ to boost oxygen evolution reaction. *Chem. Eng. J.* **2023**, *451*, 138743. DOI:10.1016/j.cej.2022.138743
20. Zhao G, Li M, Li H, Ping Z, Wang P, Wu Y, et al. La-doped micro-angular cube $ZnSnO_3$ with nano-La_2O_3 decoration for enhanced ethylene glycol sensing performance at low temperature. *Sens. Actuators A Phys.* **2023**, *362*, 114649. DOI:10.1016/j.sna.2023.114649
21. Ganta DD, Hirpaye BY, Raghavanpillai SK, Menber SY, Hahn JR. Green Synthesis of Hydroxyapatite Nanoparticles Using Monoon longifolium Leaf Extract for Removal of Fluoride from Aqueous Solution. *J. Chem.* **2022**, *2022*, 4917604. DOI:10.1155/2022/4917604
22. Scheverin VN, Horst MF, Lassalle VL. Novel hydroxyapatite-biomass nanocomposites for fluoride adsorption. *Results Eng.* **2022**, *16*, 100648. DOI:10.1016/j.rineng.2022.100648
23. Sekar S, Panchu SE, Kolanthai E, Rajaram V, Subbaraya NK. Enhanced stability of hydroxyapatite/sodium alginate nanocomposite for effective fluoride adsorption. *Mater. Today Proc.* **2022**, *58*, 909–917. DOI:10.1016/j.matpr.2021.12.064
24. Jeyaseelan A, Viswanathan NJI, Research EC. Investigation of Hydroxyapatite-Entrenched Cerium Organic Frameworks Incorporating Biopolymeric Beads for Efficient Fluoride Removal. *Ind. Eng. Chem. Res.* **2022**, *61*, 7911–7925. DOI:10.1021/acs.iecr.2c00487
25. Huang S, Hu M, Li D, Wang L, Zhang C, Li K, et al. Fluoride sorption from aqueous solution using $Al(OH)_3$-modified hydroxyapatite nanosheet. *Fuel* **2020**, *279*, 118486. DOI:10.1016/j.fuel.2020.118486
26. Laonapakul T, Suthi T, Otsuka Y, Mutoh Y, Chaikool P, Chindaprasirt P. Fluoride Adsorption Enhancement of Calcined-Kaolin/Hydroxyapatite composite. *Arab. J. Chem.* **2022**, *15*, 104220. DOI:10.1016/j.arabjc.2022.104220
27. Yapo NZS, Aw S, Briton BGH, Drogui P, Yao KB, Adouby K. Removal of fluoride in groundwater by adsorption using hydroxyapatite modified Corbula trigona shell powder. *Chem. Eng. J. Adv.* **2022**, *12*, 100386. DOI:10.1016/j.ceja.2022.100386
28. Huang J, Liu T, Zhang Y, Hu P. Reinforced adsorption mechanism of fluorine ions by calcium-depleted hydroxyapatite and application in the raffinate from the vanadium industry. *Chem. Eng. J.* **2023**, *452*, 139379. DOI:10.1016/j.cej.2022.139379
29. Nijhawan A, Butler EC, Sabatini DA. Fluoride Adsorption on Porous Hydroxyapatite Ceramic Filters: A Study of Kinetics. *Environ. Eng. Sci.* **2020**, *37*, 409–416. DOI:10.1089/ees.2019.0392

30. Mchich Z, Aziz K, Kjidaa B, Saffaj N, Saffaj T, Mamouni R. Eco-friendly engineering of micro composite-based hydroxyapatite bio crystal and polyaniline for high removal of OG dye from wastewater: Adsorption mechanism and RSM@BBD optimization. *Environ. Res.* **2024**, *257*, 119289. DOI:10.1016/j.envres.2024.119289
31. Cheikh S, Imessaoudene A, Bollinger JC, Manseri A, Bouzaza A, Hadadi A, et al. Adsorption behavior and mechanisms of the emerging antibiotic pollutant norfloxacin on eco-friendly and low-cost hydroxyapatite: Integrated experimental and response surface methodology optimized adsorption process. *J. Mol. Liq.* **2023**, *392*, 123424. DOI:10.1016/j.molliq.2023.123424
32. Li S, Du K. Self-sacrificing template synthesis of ultralight porous hydroxyapatite microtube-based ceramics for hemoglobin adsorption. *Chem. Eng. J.* **2024**, *492*, 152404. DOI:10.1016/j.cej.2024.152404
33. Wang Y, Wang C, Huang X, Zhang Q, Wang T, Guo X. Guideline for modeling solid-liquid adsorption: Kinetics, isotherm, fixed bed, and thermodynamics. *Chemosphere* **2024**, *349*, 140736. DOI:10.1016/j.chemosphere.2023.140736
34. Mokhati A, Kecira Z, Benturki O, Bernardo M, Sellaoui L, Mechi N, et al. Insights into nitrobenzene adsorption mechanism on apricot stone activated carbon: A study via statistical physics models and thermodynamic analysis. *Colloids Surf. A Physicochem. Eng. Asp.* **2024**, *691*, 133864. DOI:10.1016/j.colsurfa.2024.133864
35. Wu G, Zhao R, Li X. Response to "Comment on Magnetic tubular nickel@silica-graphene nanocomposites with high preconcentration capacity for organothiophosphate pesticide removal in environmental water: Fabrication, magnetic solid-phase extraction, and trace detection" [J. Hazard. Mater. 457 (2023) 131788]. *J. Hazard. Mater.* **2024**, *464*, 132926. DOI:10.1016/j.jhazmat.2023.132926
36. Tran HN, Lima EC, Juang R-S, Bollinger J-C, Chao H-P. Thermodynamic parameters of liquid–phase adsorption process calculated from different equilibrium constants related to adsorption isotherms: A comparison study. *J. Environ. Chem. Eng.* **2021**, *9*, 106674. DOI:10.1016/j.jece.2021.106674
37. Hamri N, Imessaoudene A, Bouchelkia N, Boudraa R, Cheikh S, Bollinger JC, et al. Innovative surface modification of Kaolinite by direct grafting of an anionic surfactant to improve pollutant adsorption and effluent decontamination. *J. Dispers. Sci. Technol.* **2024**, 1–20. DOI:10.1080/01932691.2024.2448761
38. Imessaoudene A, Cheikh S, Bollinger JC, Belkhiri L, Tiri A, Bouzaza A, et al. Zeolite Waste Characterization and Use as Low-Cost, Ecofriendly, and Sustainable Material for Malachite Green and Methylene Blue Dyes Removal: Box–Behnken Design, Kinetics, and Thermodynamics. *Appl. Sci.* **2022**, *12*, 7587. DOI:10.3390/app12157587
39. Adamu DB, Tufa LT, Lee J, Zereffa E, Segne TA, Razali MH. Facile synthesis of bismuth and iron co-doped hydroxyapatite nanomaterials for high-performance fluoride ions adsorption. *J. Environ. Chem. Eng.* **2023**, *11*, 111196. DOI:10.1016/j.jece.2023.111196
40. Mahmood BK, Kareem RO, Bulut N, Ates T, Keser S, Kaygili O, et al. Structural, magnetic, thermal, biocompatibility, and electronic properties of lanthanum doped-magnesium hydroxyapatite. *Ceram. Int.* **2025**, *51*, 18607–18616. DOI:10.1016/j.ceramint.2025.02.041
41. Li B, Chen H, Yuan X. Influence of different La_2O_3 loading on hydroxyapatite supported nickel catalysts in the dry reforming of methane. *Fuel* **2024**, *369*, 131687. DOI:10.1016/j.fuel.2024.131687
42. Sun X, Ke C, Lu Q, Wang Q, Zhou S, Liang L, et al. Recent Advances in Adsorption Techniques for the Removal of Fluoride Ions from Wastewater: A Review. *Ind. Eng. Chem. Res.* **2024**, *63*, 19936–19954. DOI:10.1021/acs.iecr.4c02734
43. Sinharoy A, Chung CM. Fluoride removal from wastewater and potential for resource recovery: Comparative studies between different treatment technologies. *Environ. Eng. Res.* **2024**, *29*, 240179-0. DOI:10.4491/eer.2024.179